Mechanistic evidence that motif-gated domain recognition drives contact prediction in protein language models

Jatin Nainani[1], **Bryn Marie Reimer**[1], **Connor Watts**[2], **David Jensen**[1], **Anna G. Green**[1]
[1]Manning College of Information and Computer Sciences,
University of Massachusetts, Amherst
[2]Queen Mary University of London
{jnainani,breimer,jensen,annagreen}@umass.edu, c.watts@qmul.ac.uk

Abstract

Protein language models (pLMs) achieve state-of-the-art performance on protein structure and function prediction tasks, yet their internal computations remain opaque. Sparse autoencoders (SAEs) have been used to recover sparse features, called latents, from pLM layer representations, whose activations correlate with known biological concepts. However, prior work has not established which model concepts are *causally necessary* for pLM performance on downstream tasks. Here, we adapt causal activation patching to the pLM setting and perform it in SAE latent space to extract the minimal circuit responsible for accuracy in a contact prediction task for two case study proteins. We observe that preserving only a tiny fraction of latent–token pairs (0.022% and 0.015%) is sufficient to retain contact prediction accuracy in a residue unmasking experiment. Our circuit indicates a two-step computation in which early-layer *motif detectors* respond to short local sequence patterns, gating mid-to-late *domain detectors* which are selective for protein domains and families. Path-level ablations confirm the causal dependence of domain latents on upstream motif latents. To evaluate these components quantitatively, we introduce two diagnostics: a *Motif Conservation Test* and a *Domain Selectivity Framework* that supports hypothesis-driven tests. All candidate motif-detector latents pass the conservation test, and 18/23 candidate domain-detector latents achieve AUROC $\geq$ 0.95. To our knowledge, this is the first circuits-style causal analysis for pLMs, pinpointing the motifs, domains, and motif-domain interactions that drive contact prediction in two specific case studies. The framework introduced herein will enable future mechanistic dissection of protein language models. Code available at `https://github.com/NainaniJatinZ/plm_circuits`

1 Introduction

Protein language models (pLMs) now sit at the core of modern computational biology, achieving strong performance at many computational biology tasks [Lin et al., 2023a, Wu et al., 2022, Elnaggar et al., 2022, Nijkamp et al., 2023, Ullanat et al., 2025]. Yet, we know little about the computational mechanisms that enable these networks to transform raw amino acid sequences into higher-level structural or functional inferences. Without insight into a model's internal computations, we cannot effectively reason about predictions, debug systematic errors, or extract new biological insights.

The field of mechanistic interpretability provides insight into model computations by reverse-engineering neural networks at feature-level resolution. A central obstacle is that most neu-

39th Conference on Neural Information Processing Systems (NeurIPS 2025) Workshop: Mechanistic Interpretability.

rons in large language models are polysemantic: a single neuron fires for several unrelated sequence features [Olah et al., 2020, Elhage et al., 2022], which hampers interpretation. *Sparse autoencoders* (SAEs) project the dense activations of neurons in a large language model into a higher-dimensional sparse space, where eachneuron—called a latent—is intended to fire selectively for a single concept [Bricken et al., 2023, Gao et al., 2024, Templeton, 2024]. Efforts to port SAEs to biological sequence models have provided descriptive evidence that pLMs contain features for sequence motifs, secondary-structure elements, and whole protein families [Simon and Zou, 2024, Adams et al., 2025, Gujral et al., 2025]. While SAEs can reveal some of the concepts that a model encodes, only causal interventions—perturbing a latent's activation and measuring the effect on the output—can tell us whether a model's output depends on that concept (as encoded by a specific latent) to make predictions [Vig et al., 2020].

Here, we extend the causal interpretability framework [Lindsey et al., 2025] to SAE latents in pLMs. We study the residue–residue contact prediction capabilities of ESM-2, using causal activation patching to measure the contribution of each interpretable SAE latent. We show that contact prediction depends on only a small subset of representations by identifying specific latents, active at specific token positions, that are individually necessary. We provide evidence that the causally necessary representations correspond to biologically meaningful concepts. We show that early layers detect short sequence motifs that causally gate domain recognition in deeper layers, forming a multi-step computational circuit. By tracing ESM-2's contact prediction for specific proteins back to a compact and interpretable subgraph of the model, and by publishing the tools needed to extend this analysis, we advance the theory and practice of mechanistic understanding of protein language models.

2 Results

2.1 A framework for causal circuit discovery in pLMs

Here we outline a framework for causal circuit discovery in pLMs, building on established interpretability practice in language models [Wang et al., 2022, Lindsey et al., 2025]. Our analysis follows four steps: (i) represent hidden activations in an interpretable sparse latent space, (ii) define a task for the pLM of interest to perform, (iii) perform causal interventions in the interpretable latent space to perturb performance of the task, and (iv) interpret the biological meaning, if any, of the observed causal latents. We briefly describe each choice below.

(i) Sparse autoencoders provide an interpretable latent space for pLMs. Recent studies [Adams et al., 2025, Simon and Zou, 2024, Gujral et al., 2025] have shown that sparse autoencoders (SAEs) [Elhage et al., 2022] project the dense, polysemantic activations of protein language models into interpretable sparse representations where individual neurons, called latents, capture meaningful biological concepts. We use SAEs from Adams et al.: eight layers (4–32 in steps of 4), 4,096 latents each.

(ii) Contact prediction as an example task for PLMs. An ideal downstream task for activation patching to interpret pLM behavior is one in which the model exhibits a near-discrete behavior switch over a small change in input, because this minimizes possible confounds[Zhang and Nanda, 2023, Wang et al., 2022]. Such behavior has been documented for the residue-residue contact prediction capabilities of ESM-2-3B. Zhang et al. showed that contact recovery for distant secondary-structure elements (SSEs) in a partially masked sequence stays near random until a critical number of residues flanking the SSEs are unmasked; then accuracy "jumps" to near-perfect (Fig. 1A-C). This results in two nearly identical inputs for which the network has a major transition in its output. We select two such case-study proteins: MetXA (UniProt: P45131), where unmasking two additional residues raises the contact recovery score $m(X)$ from 0.02 to 0.58; and TOP2 (UniProt: P06786), where unmasking four extra residues raises $m(X)$ from 0.06 to 0.86.

(iii) Activation patching to identify causal network components. Activation patching [Vig et al., 2020, Finlayson et al., 2021] can measure the causal necessity of every latent, at each token position (which we call "latent-token pair") for a specific task and input pair. For each case study input pair, we define the *corrupted input* as the input sequence and with low contact recovery, and the *clean input* as the related sequence and with high recovery. The corresponding latent activations

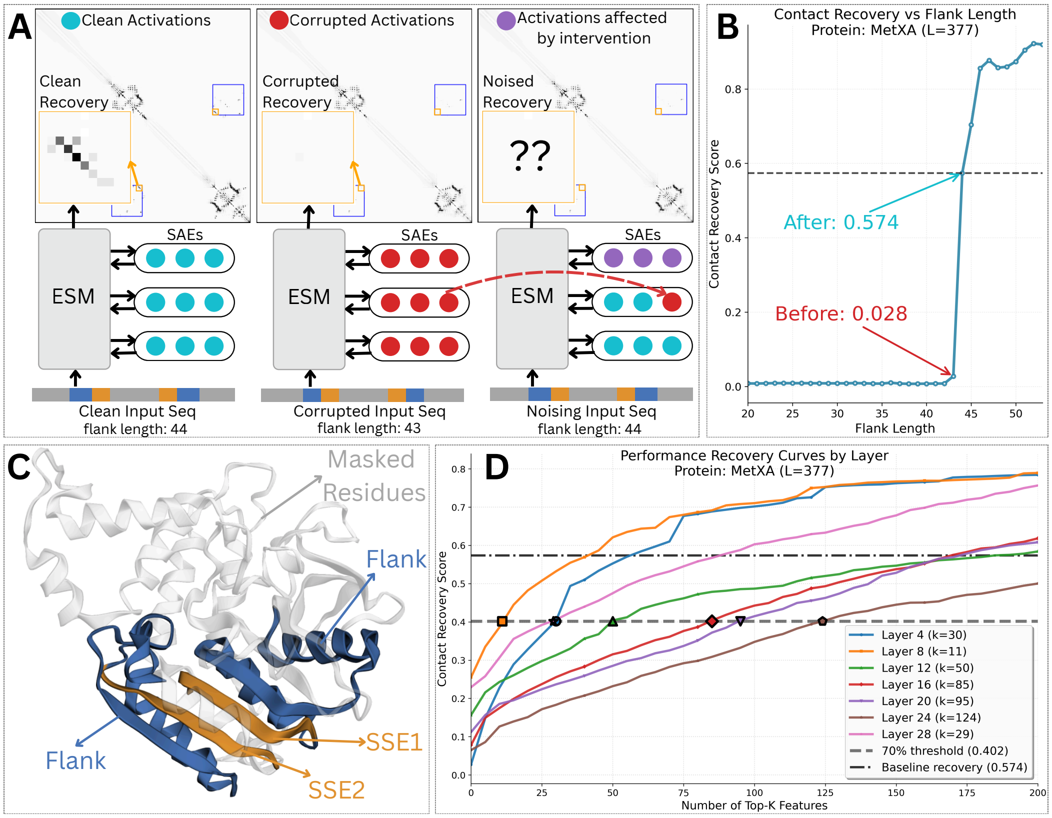

Figure 1: **(A)** Residue-residue contact maps for MetXA under three conditions: clean sequence (44 aa) yields near-perfect recovery; corrupted sequence (43 aa) yields near-random contact recovery; causal intervention replaces clean activation with a single latent patched to its corrupted value. Loss of contact recovery flags that latent as causal. **(B)** Contact recovery jump behavior reproduced from Zhang et al. [2024]. **(C)** MetXA structure (RCSB-PDB ID: 2B61 Chain A [Mirza et al., 2005]); the studied SSE elements are highlighted in yellow. **(D)** Recovery vs. per-layer circuit size. Starting points differ by error-node performance m_0.

are also called corrupted and clean, respectively. We use activation patching to compute the Indirect Effect (IE), which measures the causal influence of the input on the output through a single latent acting as a mediator Pearl [2022], by patching corrupted activations into a clean pass of the model to determine whether specific latent-token pairs were causally necessary for the task (Methods, Sec. 4; Fig. 1A). We identify a "circuit": the smallest set of latents whose clean activations sustain contact recovery (Sec. 2.2). We later extend this analysis to interactions between components (Sec. 2.4.3).

(iv) Interpretation of causal network components After identification of relevant latent-token pairs, we ask what biological computations they represent and how they interact to produce the jump in conctact recovery. We proceed in two stages. First, we assign *global* semantic labels by inspecting each latent's top-activating residues and proteins across the corpus. Second, we characterize each latent's *task-specific role* by comparing its activation in the clean vs. corrupted inputs around the flanking regions that control the jump. From these observations we formulate hypotheses about: (i) the function of individual latents; and (ii) directed interactions between latents across layers (Sec. 2.3). We then attempt to falsify these hypotheses using targeted interventions and selectivity tests (Sec. 2.4).

2.2 Causal circuits underlying contact prediction for two case study proteins

We compute the indirect effect (IE) for 4,096 latents across 8 layers at ∼400 token positions ($\approx 1.3 \times 10^7$ latent–token pairs), and then compute both global and layer-wise circuits.

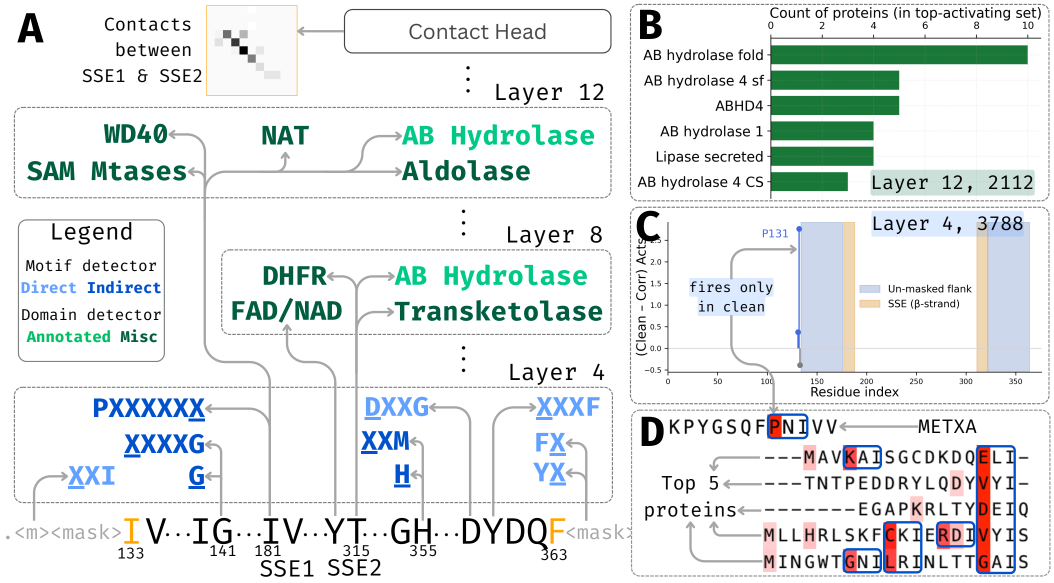

Figure 2: **(A)** Motif and domain detectors in the layer-wise circuit for MetXA. Arrows connect causal latent-token pairs. **(B)** Frequency of Interpro domains for top 10 proteins with highest activation for latent 2112 in layer 12. **(C)** Change in activation of latent 3788 in layer 4 from clean to corrupted. The latent-token pair at position P131 only activates when I133 is unmasked in the clean sequence supporting motif activation of $\underline{X}$XI. **(D)** Screenshot of activation patterns of the top 5 proteins for latent 3788 in layer 4 from Interprot [Adams et al., 2025].

Global circuits for quantification We ask for the smallest subset K of latent–token pairs whose clean activations keep contact recovery above a threshold θ of the clean score (Fig. 1D). For each protein, we fix the threshold at 70% of the clean contact recovery, $\theta = 0.70 \times m_{\text{clean}}$. Then, for a given K, we patch all non–top K pairs to their corrupted activations, recompute the model, and check whether $m(X) \geq \theta$; if so, those K latent-token pairs are sufficient (Sec. 4). Fig. 13a and Fig. 14a show the increase in $m(X)$ with increasing top K pairs considered. For both proteins, only a tiny subgraph is needed for the circuit to reach the 70%-of-clean threshold θ: 2,401 pairs (0.022%) for MetXA and 1,801 (0.015%) for TOP2. Thus the contact-prediction switch is governed by a subgraph three orders of magnitude smaller than the full network.

Layer-wise circuits for interpretability Manually inspecting thousands of pairs is infeasible without a prior, so we analyze one layer at a time. For layer ℓ, the bottleneck $\mathcal{B}_\ell$ is the smallest within-layer subset that maintains $m(X) \geq \theta$ with all other layers left unmodified. Because the SAEs cannot perfectly reconstruct activations, SAEs include an "error" node that carries reconstruction loss [Marks et al., 2024]. For layer ℓ, let the zero-circuit performance $m_0(\ell)$ be the score when all pairs in that layer are patched to their corrupted values and only the error node remains active. Because this node contains the activations "unexplained" by the SAE, we treat it as non-interpretable; continuing work aims to reduce its contribution [Rajamanoharan et al., 2024, Bussmann et al., 2024]. We focus on the *explainable window* $W_\ell = \theta - m_0(\ell)$, the margin above the error-only baseline that a layer's bottleneck must account for; we report drops both in absolute units and as a percent of W_ℓ. The resulting bottlenecks $\mathcal{B}_\ell$ contains on average only ≈ 60 latent–token pairs—tractable for qualitative study yet still drawn from the very top of the global IE ranking (Fig. 1D).

2.3 Manual inspection of two case studies reveals a motif-gated, domain-recognition circuit

We now manually annotate the causally relevant latents in each layer-wise bottleneck for both of our case study proteins. Manual annotation in this step will be used to generate hypotheses that are quantitatively tested in the next step. For every latent–token pair in each layer's bottleneck we ask two questions. First, (Q1) what biological signal, if any, does the latent usually represent? Second, (Q2) how does that latent's activation change from the corrupted to the clean input, and why might that change unblock the downstream domain detector? We answer both questions by (E1) inspecting the 20 UniRef50 proteins that most strongly activate the latent and (E2) comparing the latent's activation maps between corrupted and clean runs of the case-study protein (Sec. 4). We describe motifs using the following notation: specific residues use one-letter amino-acid codes; *X* denotes any residue; an underline marks the token where the latent activates (e.g., XXI indicates a latent that activates two residues upstream of an isoleucine). See Sec. B.3 for details.

2.3.1 Homoserine *O*-acetyltransferase

Unmasking I133 (left) and F363 (right) raises contact recovery from $m_{\text{corr}} = 0.02$ to $m_{\text{clean}} = 0.58$ ($\Delta m = 0.56$); thus the threshold $T = 0.40$. We provide per-latent and per-latent-cluster details in Table 1 and Table 3 respectively. Latents not detailed could not readily be assigned a global or task-specific role by manual inspection.

Layer 4. The zero-circuit performance $m_0 = 0.027$, thus the explainable window $W = T - m_0 = 0.373$. The circuit requires 30 latent–token pairs to meet the criterion. We find latents that activate on short sequence patterns (Q1) across the proteome (E1), so we label them *motif detectors*. This cluster contains 10 pairs (33.33% of the layer). We identify *direct* motif detectors that include one of the two newly unmasked residues (16.67% of layer). Ablating them reduces $m(X)$ by 22.9% of W (0.0863). For example, a latent at P131 fires on the motif XXI across its top 20 activating proteins (E1, Fig. 2D) and switches on only when I133 is revealed (E2→Q2, Fig. 2C). We also identify *indirect* motif detectors, which activate on residues not in the flank region, but whose activation differs between corrupted and clean inputs (16.67% of layer). Ablating them reduces $m(X)$ by 13.3% of W (0.0501). Example: a latent at I181 (center of SSE1) activates for PXXXXXX (E1); its activation rises once distant flanks are unmasked (E2→Q2). Together, motif detectors account for 35% of W (0.132).

Layer 8. The zero-circuit performance is $m_0 = 0.255$, thus the explainable window $W = T - m_0 = 0.145$. The circuit requires 11 latent–token pairs to meet the criterion. We observe latents which which activate on proteins (Q1) containing a specific domain annotation, and term them *domain detectors*. This cluster contains 5 pairs (45.45% of the layer). Domains matching MetXA 's own annotation (*annotated* domain detectors) comprise 9.09% of layer, and ablating them reduces $m(X)$ by 9.54% of W (0.015). We also see latents that activate on other domains (*miscellaneous* domain detectorrs), such as DHFR, FAD/NAD, or transketolase domains (E1) (36.36% of layer). Ablating them reduces $m(X)$ by 38% of W (0.0597), suggesting the model cross-checks related folds. Together, domain detectors account for 47.2% of W (0.0742).

Layer 12. The zero-circuit performance is $m_0 = 0.156$, thus the explainable window $W = T - m_0 = 0.244$. The circuit requires 50 latent–token pairs to meet the criterion. Similar to Layer 8, Layer 12 contains *domain detectors*. The group of domain detectors comprises 8 pairs (16% of the layer). *Annotated* domain detectors comprise 4% of the layer, and ablating them reduces $m(X)$ by 7.74% of W (0.0192). For example, a latent selective for the AB-hydrolase fold (E1, Fig. 2B) is causal at two token positions. *Miscellaneous* domain detectors activate on NAT, SAM-methyltransferase, WD40, and aldolase families (E1) (12% of layer). Ablating them reduces $m(X)$ by 29.11% of W (0.072). Together, domain detectors account for 37.7% of W (0.093).

2.3.2 DNA topoisomerase 2

Unmasking T31–Y32 (left) and G271–E272 (right) raises contact recovery from $m_{\text{corr}} = 0.06$ to $m_{\text{clean}} = 0.86$ ($\Delta m = 0.80$); threshold $T = 0.6$. Per-cluster and per-latent details are in Table 2 and Table 4. SAE error nodes already achieve $m_0 = 0.59$ at Layer 8 ($> T$), so we analyze Layers 4, 12, and 16 where $W > 0$. As in MetXA, Layer 4 contains motif detectors and Layers 12/16 contain domain detectors. The novelty is not the presence of these two functional classes but their reappearance with protein-appropriate content: TOP2's Layer 4 motifs differ from MetXA's, and its domain detectors align with TOP2's GHKL/HATPase_c annotation. We cover the per-layer analysis in the Appendix A.

2.3.3 Shared mechanism and hypotheses.

Across both proteins, we observe that early layers (L4) contain motif detectors; mid/late layers (L8-16) contain domain detectors. Unmasking flank residues raises activation in both *direct* and *indirect*

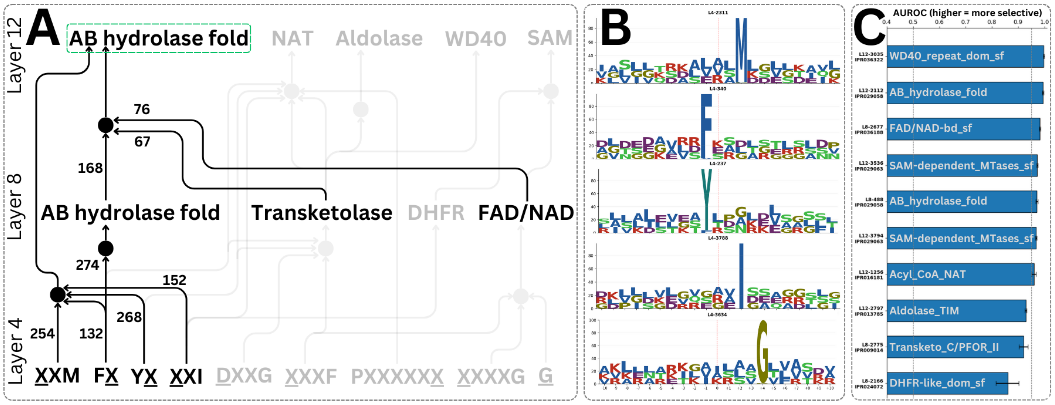

Figure 3: **(A)** Circuit diagram for MetXA with causal edges between latents. The subgraph for AB hydrolase is highlighted for readability, with edge ranks (out of 1580) shown. **(B)** Sequence logos for hypothesized motif detectors. **(C)** AUROC scores for hypothesized domain detectors. Label on the bar denotes the "short name" on Interpro.

motif detectors, and domain detectors. The reason for activation of indirect motif detectors and domain detectors is not readily obvious, but one hypothesis is that the motif detectors give signal to the domain detectors. Because the explainable windows reported here are layer-specific and not cumulative, we test end-to-end causal gating with path-level ablations in Sec. 2.4.3.

Together, the case studies suggest a two-step circuit, that we hypothesize works in the following way: (1) early-layers require latents that detect specific motifs, (2) later layers require latents that detect specific domains, and (3) domain recognition is causally gated by the early layer motif detectors.

2.4 Quantitative validation of mechanistic hypotheses

In this section, we subject our hypotheses from the case studies to quantitative validation.

2.4.1 Motif detectors preferentially activate on assigned motifs

Our case studies suggested that Layer 4 latents function as specific motif detectors which trigger the contact prediction circuit. We now ask whether each latent does indeed fire on a specific motif across all proteins, not just for our specific case study proteins.

We sample 10,000 proteins from the set of UniProt reviewed proteins and record the activation for each latent for each input token (Sec. 4.2.1). For every latent in our layer-specific bottlenecks, we create a sequence logoby recording the window around top activating token for each protein. For each latent in our qualitative analysis that was seen to be associated with a particular motif, that motif was also present in the sequence logo and accounted for more than 50% of the information at each position. As shown in Fig 3, we see that the residue that is fixed for a motif (*e.g.* F in XXXF) and its position are highly conserved whereas the rest of the window is not. All sequence logos are displayed in Fig. 5 and 6.

We found motif detectors not annotated during the manual analysis, including F (Layer 4, 181), FXXXX (Layer 4, 1096), and DXXX (Layer 4, 1712). The SAE latents we identified as motif detectors behave as motif detectors across the proteome, not just in our specific case study proteins.

2.4.2 Domain detectors preferentially activate on assigned domains

Our case studies identified causally important latents that seem to be associated with protein domains; we tested whether 23 pre-specified latent-to-domain hypotheses (10 in MetXA, 13 in TOP2) hold on the full set of reviewed Uniprot protein entries, using length-matched negatives. Because latents activate on a per-token basis and domains are a protein-level feature, we compute a protein-level latent activation score by taking the mean of the activation on the top-q% (where q=1) of tokens for that latent. We report AUROC ± 95% stratified confidence intervals to test how selective a latent

z is for domain d (Sec. 4.2.2). We found that 7/10 latent-to-domain hypotheses for MetXA and 10/13 for TOP2 had AUROC > 0.95 (95% CI width ± 0.02). In MetXA, these were latents selective for AB hydrolase fold, FAD/NAD, NAT, SAM Mtases, and WD40. For TOP2, latents with high AUROC were associated with Kinesin, HATPase_c, and XPG_I. A few tests returned moderate AUROC results (e.g., MetXA Transketolase AUC 0.92, DHFR 0.86, Aldolase 0.93; TOP2 two HATPase_c latents at 0.71 and 0.79), suggesting these latents may be non-specific or non-selective in some way. We note that choice of the protein-level latent activation score affects the conclusions (Figs. 7, 8,and 9). We found that the global mean dilutes signal of sparse detectors in long sequences; the max and top-K are length-biased. The top-q score captures signal for both sparse and dense detectors and is not length-biased.

2.4.3 Domain detectors are dependent on motif detectors

We hypothesized from the case studies that domain detectors are causally gated by motif detectors. That is, the presence of specific motifs allows the model to detect the domain/family of the protein. To test this we use *path patching* [Wang et al., 2022]: (1) patch the earlier feature to its corrupted value and record the value the later feature takes; (2) in a new run, set only that later feature to the recorded value and measure the change in contact recovery. This isolates the effect flowing along that specific link; we report edge strength as $|\Delta m|$. (Sec. B.5.3)

We rank edges by absolute effect $|\Delta m|$ and compute the cumulative area under the sorted curve $A(k) = \sum_{i=1}^{k} |\Delta m|_i$ (Fig. 10, 11). We choose the smallest k such that $A(k) \geq 0.75 \times A(\text{all})$. Under this rule, MetXA requires $k = 316/1580$ edges (20.0%) to cover 76.5% AUC, and TOP2 requires $k = 244/1064$ edges (22.9%) to cover 75.4% AUC.

Homoserine *O*-acetyltransferase Within the AUC-75% set (316 edges; 20.0% of 1580), we find *28* edges between labeled components (Table 7), including multiple motif→domain links consistent with gating. For example, motif detectors for F$\underline{\text{X}}$, $\underline{\text{X}}$XI, $\underline{\text{X}}$XM, and Y$\underline{\text{X}}$ connect to AB-hydrolase detector (2112) in Layer 12 (Fig. 3)Most late-layer domain detectors receive at least one motif detector input in this set; one Layer-12 domain detector lacks a direct motif edge but connects via another Layer-12 domain that *does* receive motif input, consistent with motif-gated recognition through an intermediate domain.

DNA topoisomerase 2 Within the AUC-75% set (244 edges; 22.9% of 1064), we observe *39* edges between labeled components (Table 8). As a representative example, several Layer-4 motif detectors converge on a *single* HATPase_c detector (1166) in Layer 16—$\underline{\text{E}}$, $\underline{\text{X}}$N, $\underline{\text{X}}$XQ, $\underline{\text{V}}$ D$\underline{\text{X}}$, $\underline{\text{X}}$XXN, and G$\underline{\text{X}}$—with ranks 46, 66, 79, 100, 189, 225, and 229, respectively. Other HATPase_c and Kinesin detectors in Layers 12 and 16 also receive motif detector inputs (see Table 8). All but one late-layer domain detector have a direct motif input within this set; the remaining detector has no labeled inbound edges.

3 Discussion

We provide the first example of circuit analysis for pLMs, by adapting the causal intervention framework from mechanistic interpretability. We demonstrate how causal intervention on SAE latents using clean/corrupted input pairs can help identify the internal circuits used by pLMs to perform a downstream task. While we apply our framework to contact prediction in ESM, it is readily generalizable to other pLMs and tasks. For our case study proteins, we show that preserving only a tiny fraction of latent–token pairs is sufficient to retain most post-jump accuracy. We observe a small set of early-layer latents that respond to short sequence motifs, that gate mid-to-late latents selective for protein domains/families, as confirmed by path-level ablations. We emphasize that these links are *model-internal* causal dependencies under our perturbation scheme ; our work does not address *biochemical* mechanism or causality.

Identifying and labeling causally-relevant latent-token pairs could enable new forms of discovery with pLMs. First, we can check whether model predictions rely on biologically sensible evidence. Second, we can investigate targeted editing and steering: attenuating misleading latents or amplifying mechanistically plausible ones, without retraining the entire model. Third, we can perform systematic follow up on cases where our labels do or do not align with known motifs and domains.

This analysis may uncover overlooked functional sites, suggest previously unrecognized domain relationships, and inspire wet-lab tests that feed back into both model refinement and biological discovery.

3.1 Limitations

Our causal claims are restricted to *where* we intervened and *what* we measured. We study ESM-2-650M because residual-stream SAEs are publicly available for this variant, but only for every four transformer blocks. For tractability we rank and evaluate layer bottlenecks for the first 3 SAE layers, and our work is restricted to contact prediction circuits in two case-study proteins. Some top-ranked latents could not be confidently labeled as motif or domain detectors. Our motif-conservation check does not perform explicit multiple-sequence alignment and may miss gapped/shifted motifs.

3.2 Future Work

Future work will expand the scope of our causal annotation for contact prediction. SAEs trained at every layer (and ideally on attention/MLP streams) or cross layer transcoders [Lindsey et al., 2025], would enable cross-layer minimal-set searches for the full circuit. Extending our analysis from the flank-induced jumps to full input sequences will test whether the same motif $\rightarrow$ domain logic persists when many residue pairs are jointly scored, and whether additional long-range features emerge. Finally, rather than summarizing interventions with a single scalar, we will analyze *per-contact* effects: which residue pairs gain/lose probability under targeted latent edits, how these changes cluster in 2D contact space (e.g., within/between SSEs), and how they project to 3D via structure prediction.

We plan automated labeling of latent-token pairs to reduce manual effort and improve label reliability. We will then seek to generalize across proteins and scales, to reveal which motif/domain detectors and dependencies are shared vs. protein-specific, how they shift with model size, and whether "domain-labeled" late-layer units sometimes act as short-motif proxies.

Together, these directions take us from a tractable layer-wise bottleneck to a complete, cross-layer circuit for contact prediction, and from two case studies toward a library of mechanistic explanations that are auditable, reusable, and biologically informative.

4 Methods

In this section, we cover the methods used for case study analysis §2.3 and selectivity tests §2.4.1,2.4.2. We overview the model and data selection in Appendix §B.1, contact prediction task in Appendix §B.2, the causal intervention framework in Appendix §B.5.

4.1 Latent Interpretation and Case-Study Analysis

Each latent–token pair in the layer-wise bottlenecks was manually examined for two complementary properties: its global role and its jump-specific role. For the global role, we select the 20 UniRef50 proteins with the highest activation for the latent, and load them in the InterProt viewer [InterProt Team, 2025] [access date: June 30, 2025] annotations that overlap with the token position were retrieved automatically from UniProt and recurring sequence motifs were noted by eye. For the jump-specific role, we plotted the latent's per-token activations on the case-study protein under three inputs (corrupted, clean, and fully unmasked). The indirect-effect ranking already scales with activation change, so no additional numeric threshold was imposed. Latents whose motif encompassed a residue newly revealed in the clean input were labeled directly explained motif detectors; those whose motif lay elsewhere were labeled indirect motif detectors. Finally, latents whose activation patterns matched a specific InterPro domain—regardless of whether that domain is annotated for the target protein—were labeled domain detectors.

4.2 Quantitative latent labeling

From the full set of UniProt reviewed proteins (n = 573,661 as of June 30, 2025), we first filtered out any proteins with sequence length > 1022, as ESM-2 adds two extra tokens to the input and caps input length at 1024 tokens. Then, we randomly selected a set of 10,000 proteins from this length-restricted subset. For each of these proteins and for each available latent, the per-token activation was extracted and stored. Using the per-token activations, we then quantitatively labeled latents for both motifs and domains.

4.2.1 Motif Labeling through Sequence Conservation

To identify sequence motifs associated with latent activations, we aligned sequences at their maximum activation positions and analyzed conservation patterns in flanking regions. For each latent, we identified the highest-activating residue in each protein, ranked these maxima across the dataset, selected the top 100 residues (ensuring each protein was represented only once), and computed position-specific conservation scores to quantitatively characterize activation-associated motifs. Specifically, for each of those top 100 residues, we extract the 10 amino acids before and after it in the sequence, truncating if we run into the beginning or end of the protein. The window size was chosen empirically based on manual inspection. For each latent, we then created a sequence logo using those 100 sequences of length 21 (10+1+10). Sequence logos were generated with the LOGOMAKER Python library [Tareen and Kinney, 2020]. The x-axis of such a logo gives the sequence position, relative to the middle residue (the highest-activating residue). The y-axis of a sequence logo gives the information content in bits, where the height h of an amino acid a at position i is given by:

$$h = f_{a,i} \times \left[\log_2(s) - (H_i + e_n)\right], \quad H_i \quad = -\sum_{b=0}^{t} f_{a,i} \times \log_2\left(f_{a,i}\right), \quad e_n = \frac{1}{\ln 2}\frac{s-1}{2n} \qquad (1)$$

where $f_{a,i}$ is the relative frequency of amino acid a at position i and $s = 20$ because we are only considering the 20 canonical amino acids. The quantity H_i is the Shannon entropy or the uncertainty of position i, and e_n is the small-sample correction for an alignment of n letters (here, $n = 100$ sequences) [Schneider and Stephens, 1990]. The final sequence logos for each latent represent a statistical view of the conservation of amino acids at each position in the neighborhood of the highest-activated residue.

4.2.2 Domain labeling through correlation

Protein domains are conserved sequences associated with structure and function [Chothia, 1992], and are curated in InterPro [Blum et al., 2025]. For each latent z and domain d, we hypothesize score(X, z) is higher for proteins (X) with d than without d. We test these pre-specified latent-to-domain hypotheses on a shared dataset. For a domain d, positive examples are randomly selected from the set of UniProt reviewed proteins with domain d. We defined a candidate negative pool as reviewed Uniprot proteins without d, and length-matched negatives to positives via stratified sampling over 12 empirical length-quantile bins to remove sequence-length confounding. Quantiles are computed on the union of positive and candidate-negative lengths for that domain. Within each bin, we sampled negatives without replacement up to the number of positives in that bin; if fewer negatives were available, we took all available and accepted minor imbalance. We summarize a protein's activation score by the *mean of the top q%* of tokens, with $q = 1$ (fixed *a priori*). This captures both sparse and dense signals without being length biased. An ideal score metric should also expect low Spearman Rank Correlation rho ($\rho(\text{score}, \log L) \approx 0$) on negatives. This is because for proteins without domain d, a good per-protein score should not systematically increase/decrease with sequence length. With this setup, we calculated the AUROC using scikit-learn [Pedregosa et al., 2011] to measure the effect strength for selectivity and provide 95% stratified bootstrap confidence intervals (CIs). AUROC denotes the probability that a random positive out-scores a random negative; CIs use 3000 stratified bootstrap resamples. For comparison, we computed the same metrics for max, mean, top-K as for top-q. We found that the global mean dilutes sparse activations, while the max and top-K had higher length correlations for negatives (Appendix §D).

Acknowledgments and Disclosure of Funding

The authors thank members of the UMass SAGE lab for valuable input. This work utilized resources from Unity, a collaborative, multi-institutional high-performance computing cluster managed by

UMass Amherst Research Computing and Data. BMR was supported by the UMass Spaulding-Smith Fellowship.

References

Etowah Adams, Liam Bai, Minji Lee, Yiyang Yu, and Mohammed AlQuraishi. From mechanistic interpretability to mechanistic biology: Training, evaluating, and interpreting sparse autoencoders on protein language models. *bioRxiv*, pages 2025–02, 2025.

Matthias Blum, Antonina Andreeva, Laise C. Florentino, and *et al.* Interpro: the protein sequence classification resource in 2025. *Nucleic Acids Research*, 53(D1):D444–D456, 2025. doi: 10.1093/nar/gkae1082.

Emmanuel Boutet, Damien Lieberherr, Michael Tognolli, Michel Schneider, and Amos Bairoch. UniProtKB/Swiss-Prot. *Methods in Molecular Biology*, 406:89–112, 2007. doi: 10.1007/978-1-59745-535-0_4. URL https://pubmed.ncbi.nlm.nih.gov/18287689/.

Trenton Bricken, Adly Templeton, Joshua Batson, Brian Chen, Adam Jermyn, Tom Conerly, Nick Turner, Cem Anil, Carson Denison, Amanda Askell, et al. Towards monosemanticity: Decomposing language models with dictionary learning. *Transformer Circuits Thread*, 2, 2023.

Bart Bussmann, Patrick Leask, and Neel Nanda. Batchtopk sparse autoencoders. *arXiv preprint arXiv:2412.06410*, 2024.

Diego Caples, Jatin Nainani, Callum McDougall, and R. Renaud. Scaling sparse feature circuit finding to gemma 9b. https://www.lesswrong.com/posts/PkeB4TLxgaNnSmddg/scaling-sparse-feature-circuit-finding-to-gemma-9b, January 2025. URL https://www.lesswrong.com/posts/PkeB4TLxgaNnSmddg/scaling-sparse-feature-circuit-finding-to-gemma-9b. LessWrong post.

Cyrus Chothia. One thousand families for the molecular biologist. *Nature*, 357(6379):543–544, 1992. doi: 10.1038/357543a0.

Scott Classen, Stephane Olland, and James M Berger. Structure of the topoisomerase ii atpase region and its mechanism of inhibition by the chemotherapeutic agent icrf-187. *Proceedings of the national academy of sciences*, 100(19):10629–10634, 2003.

Nelson Elhage, Tristan Hume, Catherine Olsson, Nicholas Schiefer, Tom Henighan, Shauna Kravec, Zac Hatfield-Dodds, Robert Lasenby, Dawn Drain, Carol Chen, et al. Toy models of superposition. *arXiv preprint arXiv:2209.10652*, 2022.

Ahmed Elnaggar, Michael Heinzinger, Christian Dallago, Ghalia Rehawi, Yu Wang, Llion Jones, Tom Gibbs, Tamas Feher, Christoph Angerer, Martin Steinegger, Debsindhu Bhowmik, and Burkhard Rost. Prottrans: Toward understanding the language of life through self-supervised learning. *IEEE Transactions on Pattern Analysis and Machine Intelligence*, 44(10):7112–7127, 2022. doi: 10.1109/TPAMI.2021.3095381.

Matthew Finlayson, Aaron Mueller, Sebastian Gehrmann, Stuart Shieber, Tal Linzen, and Yonatan Belinkov. Causal analysis of syntactic agreement mechanisms in neural language models. *arXiv preprint arXiv:2106.06087*, 2021.

Leo Gao, Tom Dupré la Tour, Henk Tillman, Gabriel Goh, Rajan Troll, Alec Radford, Ilya Sutskever, Jan Leike, and Jeffrey Wu. Scaling and evaluating sparse autoencoders. *arXiv preprint arXiv:2406.04093*, 2024.

Onkar Gujral, Mihir Bafna, Eric Alm, and Bonnie Berger. Sparse autoencoders uncover biologically interpretable features in protein language model representations. *Proceedings of the National Academy of Sciences*, 122(34):e2506316122, 2025. doi: 10.1073/pnas.2506316122.

Michael Hanna, Sandro Pezzelle, and Yonatan Belinkov. Have faith in faithfulness: Going beyond circuit overlap when finding model mechanisms. *arXiv preprint arXiv:2403.17806*, 2024.

InterProt Team. InterProt Viewer: Interactive Protein Sequence and Domain Visualisation. https://interprot.com, 2025. Accessed 2 Aug 2025.

János Kramár, Tom Lieberum, Rohin Shah, and Neel Nanda. Atp*: An efficient and scalable method for localizing llm behaviour to components. *arXiv preprint arXiv:2403.00745*, 2024.

Zeming Lin, H. Joseph Akin, Roshan Rao, Brian Hie, Zhong Zhu, Will Lu, Tom Sercu, and Yang Song. Esmfold: End-to-end single-sequence structure prediction using protein language models. *Science*, 379(6637):364–369, 2023a. doi: 10.1126/science.ade2574.

Zeming Lin, Halil Akin, Roshan M. Rao, and et al. Evolutionary-scale prediction of atomic-level protein structure with a language model. *Science*, 379(6637):1123–1130, 2023b. doi: 10.1126/science.ade2574.

Jack Lindsey, Wes Gurnee, Emmanuel Ameisen, Brian Chen, Adam Pearce, Nicholas L. Turner, Craig Citro, David Abrahams, Shan Carter, Basil Hosmer, Jonathan Marcus, Michael Sklar, Adly Templeton, Trenton Bricken, Callum McDougall, Hoagy Cunningham, Thomas Henighan, Adam Jermyn, Andy Jones, Andrew Persic, Zhenyi Qi, T. Ben Thompson, Sam Zimmerman, Kelley Rivoire, Thomas Conerly, Chris Olah, and Joshua Batson. On the biology of a large language model. *Transformer Circuits Thread*, 2025. URL `https://transformer-circuits.pub/2025/attribution-graphs/biology.html`.

Samuel Marks, Can Rager, Eric J Michaud, Yonatan Belinkov, David Bau, and Aaron Mueller. Sparse feature circuits: Discovering and editing interpretable causal graphs in language models. *arXiv preprint arXiv:2403.19647*, 2024.

Meta AI (FAIR). ESM-2 Contact-Prediction Head (Logistic Regression Weights). `https://github.com/facebookresearch/esm`, 2023a. Accessed 4 Aug 2025.

Meta AI (FAIR). ESM-2 and ESMFold-v0 Model Code and Weights, 2023b. URL `https://doi.org/10.5281/zenodo.7566741`.

I Ahmad Mirza, Ishac Nazi, Magdalena Korczynska, Gerard D Wright, and Albert M Berghuis. Crystal structure of homoserine transacetylase from haemophilus influenzae reveals a new family of α/β-hydrolases. *Biochemistry*, 44(48):15768–15773, 2005.

Neel Nanda. Attribution patching: Activation patching at industrial scale. *URL: https://www. neelnanda. io/mechanistic-interpretability/attribution-patching*, 2023.

Erik Nijkamp, Jeffrey A Ruffolo, Eli N Weinstein, Nikhil Naik, and Ali Madani. Progen2: exploring the boundaries of protein language models. *Cell systems*, 14(11):968–978, 2023.

Chris Olah, Nick Cammarata, Ludwig Schubert, Gabriel Goh, Michael Petrov, and Shan Carter. Zoom in: An introduction to circuits. *Distill*, 5(3):e00024–001, 2020.

Judea Pearl. Direct and indirect effects. In *Probabilistic and causal inference: the works of Judea Pearl*, pages 373–392. 2022.

Fabian Pedregosa, Gaël Varoquaux, Alexandre Gramfort, Vincent Michel, Bertrand Thirion, Olivier Grisel, Mathieu Blondel, Peter Prettenhofer, Ron Weiss, Vincent Dubourg, et al. Scikit-learn: Machine learning in python. *the Journal of machine Learning research*, 12:2825–2830, 2011.

Senthooran Rajamanoharan, Tom Lieberum, Nicolas Sonnerat, Arthur Conmy, Vikrant Varma, János Kramár, and Neel Nanda. Jumping ahead: Improving reconstruction fidelity with jumprelu sparse autoencoders. *arXiv preprint arXiv:2407.14435*, 2024.

Roshan M. Rao, Joshua Meier, Tom Sercu, Sergey Ovchinnikov, and Alexander Rives. Transformer protein language models are unsupervised structure learners. *bioRxiv*, 2020. doi: 10.1101/2020.12.15.422761. URL `https://www.biorxiv.org/content/10.1101/2020.12.15.422761v1`.

Thomas D Schneider and R Michael Stephens. Sequence logos: a new way to display consensus sequences. *Nucleic acids research*, 18(20):6097–6100, 1990.

Elana Simon and James Zou. Interplm: Discovering interpretable features in protein language models via sparse autoencoders. *bioRxiv*, pages 2024–11, 2024.

Mukund Sundararajan, Ankur Taly, and Qiqi Yan. Axiomatic attribution for deep networks. In *International conference on machine learning*, pages 3319–3328. PMLR, 2017.

Aaquib Syed, Can Rager, and Arthur Conmy. Attribution patching outperforms automated circuit discovery, 2023. URL `https://arxiv.org/abs/2310.10348`.

Ammar Tareen and Justin B. Kinney. Logomaker: Beautiful sequence logos in Python. *Bioinformatics*, 36(7):2272–2274, 2020. doi: 10.1093/bioinformatics/btz921. URL `https://pubmed.ncbi.nlm.nih.gov/31821414/`.

Adly Templeton. *Scaling monosemanticity: Extracting interpretable features from claude 3 sonnet*. Anthropic, 2024.

Varun Ullanat, Bowen Jing, Samuel Sledzieski, and Bonnie Berger. Learning the language of protein–protein interactions. *bioRxiv*, pages 2025–03, 2025.

Jesse Vig, Sebastian Gehrmann, Yonatan Belinkov, Sharon Qian, Daniel Nevo, Yaron Singer, and Stuart Shieber. Investigating gender bias in language models using causal mediation analysis. *Advances in neural information processing systems*, 33:12388–12401, 2020.

Kevin Wang, Alexandre Variengien, Arthur Conmy, Buck Shlegeris, and Jacob Steinhardt. Interpretability in the wild: a circuit for indirect object identification in gpt-2 small. *arXiv preprint arXiv:2211.00593*, 2022.

Ruidong Wu, Fan Ding, Rui Wang, Rui Shen, Xiwen Zhang, Shitong Luo, Chenpeng Su, Zuofan Wu, Qi Xie, Bonnie Berger, et al. High-resolution de novo structure prediction from primary sequence. *BioRxiv*, pages 2022–07, 2022.

Fred Zhang and Neel Nanda. Towards best practices of activation patching in language models: Metrics and methods. *arXiv preprint arXiv:2309.16042*, 2023.

Zhidian Zhang, Hannah K Wayment-Steele, Garyk Brixi, Haobo Wang, Dorothee Kern, and Sergey Ovchinnikov. Protein language models learn evolutionary statistics of interacting sequence motifs. *Proceedings of the National Academy of Sciences*, 121(45):e2406285121, 2024.

A DNA topoisomerase 2 Layer wise analysis

Layer 4. The zero-circuit performance is $m_0 = 0.33$; thus the explainable window is $W = T - m_0 = 0.27$. The circuit requires 29 latent–token pairs to meet the criterion. Similar to the results for MetXA, observe motif detectors. This cluster contains 13 pairs (44.8% of the layer). *Direct* motif detectors (20.7% of layer). Ablating them reduces $m(X)$ by 6.3% of W (0.017). Example: a latent at G34 fires on YX$\underline{\text{X}}$ across its top-20 proteins (E1) and deactivates when Y28 is masked (E2→Q2). *Indirect* motif detectors (24.1% of layer). Ablating them reduces $m(X)$ by 11% of W (0.03). Example: a latent at I101 prefers $\underline{\text{I}}$XX (E1); its activation rises only in the clean input (E2→Q2). Together, motif detectors accounts for 19.10% of W (0.053).

Layer 12. The zero-circuit performance is $m_0 = 0.096$; thus the explainable window is $W = T - m_0 = 0.50$. The circuit requires 18 latent–token pairs to meet the criterion. This layer contains *domain detectors*. This cluster contains 5 pairs (27.8% of the layer). *Annotated* domains (TOP2 's own labels: GHKL / HATPase_c) (16.7% of layer). Ablating them reduces $m(X)$ by 24.6% of W (0.125).

Misc domains (e.g., XPG-I or Kinesin) (11.1% of layer). Ablating them reduces $m(X)$ by 1.6% of W (0.01). Example: two latents prefer XPG-I/Kinesin families (E1); removal yields a small drop. Together, domain detectors accounts for 31.3% of W (0.158).

Layer 16. The zero-circuit performance is $m_0 = 0.11$; thus the explainable window is $W = T - m_0 = 0.49$. The circuit requires 25 latent–token pairs to meet the criterion. This layer also contains *domain detectors*. This cluster contains 6 pairs (24% of the layer). *Annotated* (GHKL / HATPase_c) (24% of layer). Ablating them reduces $m(X)$ by 15.6% of W (0.0785). Example: a latent at V201 fires on GHKL proteins (E1) and activates only in the clean run (E2→Q2). Together, domain detectors accounts for 15.6% of W (0.0785).

Table 1: Layer-wise role for latents in MetXA circuit.

Layer	Role	Class	Quantity	% of Layer	Δm drop (abs)	Δm drop (rel % w/o err)
4 (Zero Circuit Baseline: 0.027)	Motif Detectors	Direct	5	16.7	0.0860	22.9
		Indirect	5	16.7	0.0500	13.3
	Total Explained	-	10	33.3	0.1330	35.3
	Unlabeled	-	20	66.6	–	–
8 (Zero Circuit Baseline: 0.255)	Domain Detectors	Annotated	1	9.1	0.0150	9.5
		Misc	4	36.7	0.0590	38.0
	Total Explained	-	5	45.4	0.0740	47.2
	Unlabeled	-	6	54.6	–	–
12 (Zero Circuit Baseline: 0.156)	Domain Detectors	Annotated	2	4.0	0.0190	7.7
		Misc	6	12.0	0.0720	29.1
	Total Explained	-	8	16.0	0.0930	37.7
	Unlabeled	-	42	84.0	–	–

Table 2: Layer-wise role for latents in TOP2 circuit.

Layer	Role	Class	Quantity	% of Layer	Δm drop (abs)	Δm drop (rel % w/o err)
4 (Zero Circuit Baseline: 0.33)	Motif Detectors	Direct	6	20.7	0.0170	6.3
		Indirect	7	24.1	0.0300	11.0
	Total Explained	-	13	44.8	0.0530	19.1
	Unlabeled	-	16	55.2	–	–
12 (Zero Circuit Baseline: 0.096)	Domain Detectors	Annotated	3	16.7	0.1250	24.6
		Misc	2	11.1	0.0080	1.6
	Total Explained	-	5	27.8	0.1580	31.3
	Unlabeled	-	13	72.2	–	–
16 (Zero Circuit Baseline: 0.11)	Domain Detectors	Annotated	6	24.0	0.0780	15.6
		Misc	-	–	–	–
	Total Explained	-	6	24.0	0.0780	15.6
	Unlabeled	-	19	76.0	–	–

Table 3: Latent census by layer (MetXA).

Layer	Latent ID	Position	Global Role	Δ Activation (clean−corr.)	Class
4	3788	P113/P131	$\underline{X}$XI	2.76	Directly explained
	1690	Y362	$\underline{X}$XXF	3.95	Directly explained
	237	E366	Y$\underline{X}$	2.63	Directly explained
	798	D361	$\underline{D}$XXG	-0.38	Directly explained
	340	E366	F$\underline{X}$	3.22	Directly explained
	2277	G159	$\underline{G}$	0.13	Indirectly modulated
	3634	G159	$\underline{X}$XXXG	0.07	Indirectly modulated
	1682	I181	PXXXXX$\underline{X}$	0.09	Indirectly modulated
	2311	H355	$\underline{X}$XM	0.08	Indirectly modulated
	3326	H355	$\underline{H}$	-0.03	Indirectly modulated
8	488	T297/T315	AB hydrolase	0.45	Annotated domain
	2677	I181	FAD/NAD	1.05	Misc domain
	2166	T315	DHFR	-0.39	Misc domain
	2775	I181,T315	Transketolase	0.46,0.38	Misc domain
12	2112	I163/I181, A167	AB hydrolase	0.86,2.3	Annotated domain
	1256	I181	FAM	1.03	Misc domain
	3794	I181	SAM Mtases	1.31	Misc domain
	3035	I181	WD40	0.6	Misc domain
	2797	I181	Aldolase	1.52	Misc domain
	3536	I181	SAM Mtases	0.96	Misc domain

Table 4: Latent census by layer (TOP2).

Layer	Latent ID	Position	Global Role	Δ Activation (clean−corr.)	Class
4	1509	E272	$\underline{E}$	10.28	Directly explained
	2511	N270	$\underline{X}$XQ	1.17	Directly explained
	2112	G34	YX$\underline{X}$	6.08	Directly explained
	3069	E272	G$\underline{X}$	6.3	Directly explained
	3544	Y32	$\underline{C}$	-1.87	Directly explained
	2929	N270	$\underline{N}$	-0.24	Directly explained
	3170	D269	$\underline{X}$N	-1.23	Indirectly modulated
	3717	V101	$\underline{V}$	-0.2	Indirectly modulated
	527	N270	D$\underline{X}$	-0.4	Indirectly modulated
	1297	I71	$\underline{I}$	-0.24	Indirectly modulated
	1468	I71	$\underline{X}$XXN	0.05	Indirectly modulated
	1196	D269	$\underline{D}$	-0.54	Indirectly modulated
	3229	V101	IX$\underline{X}$	0.06	Indirectly modulated
12	3943	V201	HATPase	3.61	Annotated domain
	1796	V201	HATPase	1.48	Annotated domain
	1204	V201	HATPase	2.01	Annotated domain
	1082	V201	XPG-I	0.58	Misc domain
	2474	V201	Kinesin	1.11	Misc domain
16	1353	V201	HATPase	5.51	Annotated domain
	1597	V201,F203	HATPase	4.53	Annotated domain
	1166	T199,V201,P205	HATPase	4.34,2.65,4.03	Annotated domain

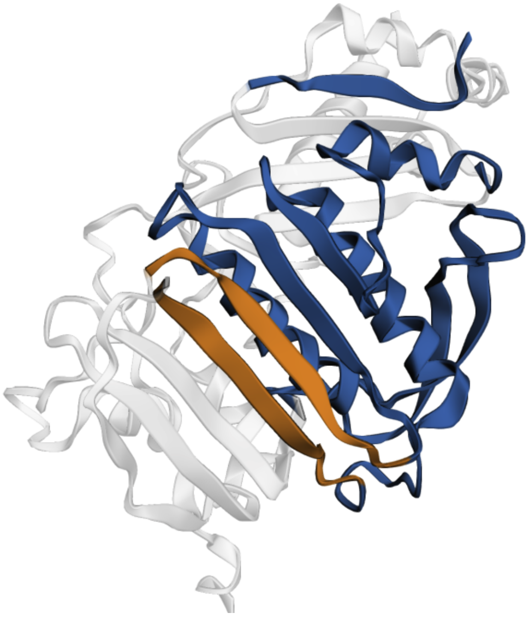

Figure 4: TOP2 structure (RCSB-PDB ID: 1PVG Chain A Classen et al. [2003]) with SSE elements used for contact prediction in orange, and relevant flank regions in blue [Zhang et al., 2024]

B Materials

B.1 Model and Data Selection

Protein language model. All experiments use ESM-2-650M as the primary protein language model, from FAIR's public repository ("esm2_t33_650M_UR50D" checkpoint). No additional fine-tuning was performed [Lin et al., 2023b, Meta AI (FAIR), 2023b].

Sparse autoencoders (SAEs). We use eight publicly released SAEs from Adams et al. [2025], trained on residual stream activations from layers 4, 8, 12, 16, 20, 24, 28, and 32. Each SAE encodes the 1 280-dimensional residual activation (extracted after the attention and MLP sublayers) to a 4 096-d latent vector z, followed by a `TopK` gate ($k = 64$) to enforce sparsity. Throughout, *latents* refers exclusively to these pretrained SAE features z.

Proteome for selectivity assays. AUROC and enrichment tests are applied to the reviewed *Swiss-Prot* subset of UniProt ($N = 573,661$ proteins) [Boutet et al., 2007]. For manual inspection of top-activating sequences we use the InterProt viewer (UR50 protein set, accessed 2 Aug 2025).

Case-study proteins. Zhang et al. [2024] demonstrated the sudden increase in contact recovery on ESM-2-3B. As both open sources SAEs were only available on ESM-2-650M, we iterated over the set of proteins from Zhang et al. [2024] and picked the two that showcased the jump in the smaller 650M model. (1) *DNA topoisomerase 2*; Species: *Saccharomyces cerevisiae strain ATCC 204508 / S288c (baker's yeast)* S288C; UniProt: P06786; PDB: 1PVG [Mirza et al., 2005] (2) *Homoserine O-acetyltransferase*; Species: *Haemophilus influenzae strain ATCC 51907 / DSM 11121 / KW20 / Rd*; UniProt: P45131; PDB: 2B61 [Classen et al., 2003].

B.2 Contact-prediction task

We adapt the contact prediction task defined by Zhang et al. [2024], using the ESM-2 contact prediction head [Rao et al., 2020, Meta AI (FAIR), 2023a]. They built a dataset of pairs of contacting secondary-structure elements (SSEs) separated by > 100 aa in the primary sequence across 266 proteins. For an input protein sequence X (which may contain masked tokens) and its corresponding pair of SSEs from their database, we define the per-SSE-pair prediction quality as the *recovery score*

$$m(X) = \frac{\sum_{i \in R_1} \sum_{j \in R_2} P(\text{contact}_{ij} \,|\, X)}{\sum_{i \in R_1} \sum_{j \in R_2} P(\text{contact}_{ij} \,|\, X_{\text{full}})}, \tag{2}$$

where R_1, R_2 index the two SSEs and X_{full} is the unmasked sequence.

Jump setup. Two inputs are compared: a *clean* sequence whose flanks yield high recovery (typically, $m \approx 1$) and a *corrupted* sequence with two fewer flank residues that collapses to near-random ($m \lesssim 0.1$). The step-change constitutes is referred to as the jump.

B.3 Motif notation

We describe motifs using one-letter amino acid codes with the following notation:

- {A,C,D,E,F,G,H,I,K,L,M,N,P,Q,R,S,T,V,W,Y}: a specific, conserved amino acid.
- X: any amino acid (position not conserved).
- underline: the token at which the latent activates.

B.4 Sparse Autoencoders (SAEs)

Neurons in deep neural networks and language models are usually polysemantic, meaning that they activate on to multiple unrelated variables or concepts [Olah et al., 2020]. One potential cause of polysemanticity is superposition, where a neural network represents more independent features of the data than it has neurons for by assigning each feature its own linear combination of neurons [Bricken et al., 2023]. The work by Elhage et al. [2022] has shown how Sparse Autoencoders (SAEs) can be used to disentangle these dense representations into monosemantic neurons, which represent a single concept/variable.

We use the sparse autoencoders trained by Adams et al., which followed Gao et al., where each SAE is a linear encoder–decoder that learns a sparse, length-k latent vector z for every residual-stream activation $x \in \mathbb{R}^d$:

$$\underbrace{z_{\text{top-}k}}_{\text{sparse}} = \text{TopK}\big(W_{\text{enc}}\,(x - b)\big), \quad \hat{x} = W_{\text{dec}}\,z + b, \qquad \mathcal{L} = \|x - \hat{x}\|_2^2.$$

Individual neurons z_i in the SAE are referred to as latents. Because only the k top activating latents survive the `TopK` gate, individual latents are often monosemantic [Gao et al., 2024], making them easier to interpret or ablate.

B.5 Circuit Discovery

B.5.1 Causal influence ranking by activation patching

We aim to discover which specific latents at each sequence position (latent–token pairs) are causally necessary for the contact prediction jump. First, we conduct two forward passes of the network, one with the clean sequence that produces near-complete contact recovery, and one with the corrupted sequence that produces near-zero contact recovery. Then, for each SAE latent at each sequence position, we measure its *indirect effect (IE)* [Pearl, 2022] using counterfactual activation patching [Vig et al., 2020, Finlayson et al., 2021]. Activation patching copies the hidden activations of a single network component from one forward pass into another. Here, we copy the latent activations from the corrupted forward pass into a clean forward pass. The change in the model's output that results from patching a component is called the *indirect effect (IE)* of that component.

Indirect-effect calculation. For a component $\mathbf{a}$ we patch its activations from the failing run into the successful one and recompute the score: $m\big(X_{\text{clean}} \mid \text{do}(\mathbf{a} \leftarrow \mathbf{a}_{\text{patch}})\big)$.

$$\text{IE}(\mathbf{a}) = m\big(X_{\text{clean}} \mid \text{do}(\mathbf{a} \leftarrow \mathbf{a}_{\text{patch}})\big) - m(X_{\text{clean}}). \tag{3}$$

Patching can be restricted to a single position t by swapping only $\mathbf{a}[t]$. We refer to the activation of a latent at a specific sequence position as "latent–token pair." Components are ranked by the magnitude of their IE; a large *negative* value indicates that importing $\mathbf{a}$ from the corrupted run alone has a large negative impact on contact recovery even though the rest of the network still receives the clean input.

Directly evaluating the indirect effect in (3) for *every* latent–token pair would require a forward pass per component ($\sim 10^7$), which is infeasible. Instead, following Marks et al. [2024] we compute effects with two gradient-based approximations: **Attribution Patching** [Nanda, 2023, Syed et al., 2023, Kramár et al., 2024]: a first-order Taylor expansion around the clean run that estimates the effect of *all* components using only two forward passes and a single backward pass. **Integrated Gradients** [Sundararajan et al., 2017, Hanna et al., 2024]: a more accurate path integral of the gradient along the straight-line interpolation between patched and clean activations. We use $N{=}10$ [Marks et al., 2024] evenly spaced interpolation points, trading the extra 10 forward–backward pairs for a noticeably tighter fit than only using attribution patching Hanna et al. [2024].

B.5.2 Circuit Discovery

Circuits are a subgraph of a neural network [Olah et al., 2020, Wang et al., 2022]. In the context of this work, we define circuit as the minimal set of latent–token pairs needed to maintain a threshold of the contact recovery, while all other pairs are ablated (frozen to their corrupted activations). We rank $4{,}092 \times 8$ latents at each of the ~ 400 sequence positions for IE, yielding $\sim 1.3 \times 10^7$ latent–token pairs. However, SAEs are usually not able to reconstruct the activations with 100% accuracy. So error terms [Marks et al., 2024] are added to the reconstructions to maintain performance. Mathematically, the error term $\varepsilon(x)$ is the difference between the model and reconstructed activations: $x = \hat{x} + \varepsilon(x)$

We construct the circuit with the top K latent–token pairs with highest indirect effect. We begin by patching the corrupted activations for every pair not in the top K. Then, we allow the top K to be recomputed during the forward pass. If contact recovery jumps, the retained pairs are sufficient to create the circuit; if it remains low, the circuit is still missing critical pieces and we continue adding more clean activations. We set the threshold at 70% of the post-jump recovery. We chose 70% to explain the majority of the jump while focusing on the most important latents.

Layer-wise bottlenecks. In addition to the model-spanning circuit defined above, we seek to compute layer-specific bottlenecks, defined as the minimal set of latent–token pairs from a specific layer needed to maintain a threshold of contact recovery, with all other latent–token pairs from that layer ablated and with all other layers not directly intervened. For layer ℓ we allow only its top-K_ℓ latent–token pairs to be recomputed and patch the corrupted activation for all other latent–token pairs in that layer. All other layers are also allowed to be recomputed. Caples et al. [2025]. K_ℓ is the smallest value reaching $\geq$70% recovery, this set of pairs are referred to as $\mathcal{B}_\ell$. Layer bottlenecks trade completeness for interpretability: $\mathcal{B}_\ell \subseteq$ circuit, but each is small enough for manual inspection.

B.5.3 Path Patching

To quantify how strongly an *upstream* SAE feature u_i in layer ℓ influences a *downstream* feature d_j in layer ℓ', we follow Wang et al. [2022] and compute an *edge attribution* via *path patching*. This method isolates the causal pathway from u_i to d_j through a two-stage intervention:

1. **Record downstream change**: Patch the upstream feature activation from u_i^{clean} to u_i^{corr} while keeping all other upstream features at their clean values. Record the resulting downstream activation d_j^{ablated}.
2. **Isolate pathway effect**: In a fresh forward pass on the clean input, patch only the downstream feature from d_j^{clean} to d_j^{ablated} (the value recorded in step 1), keeping all other features at their clean values.
3. **Measure metric change**: Compute the change in metric (2): $w_{i \to j} = m_{\text{patched}} - m_{\text{clean}}$.

The resulting edge weight $w_{i \to j}$ isolates the causal contribution of feature u_i to the model's performance that flows specifically through feature d_j, excluding any parallel pathways. This two-stage patching procedure ensures we capture only the direct $u_i \to d_j$ influence, providing a precise measure of feature interaction strength. However, this needs $\mathcal{O}(K^2)$ forward passes for complete pairwise analysis.

C Sequence Logos

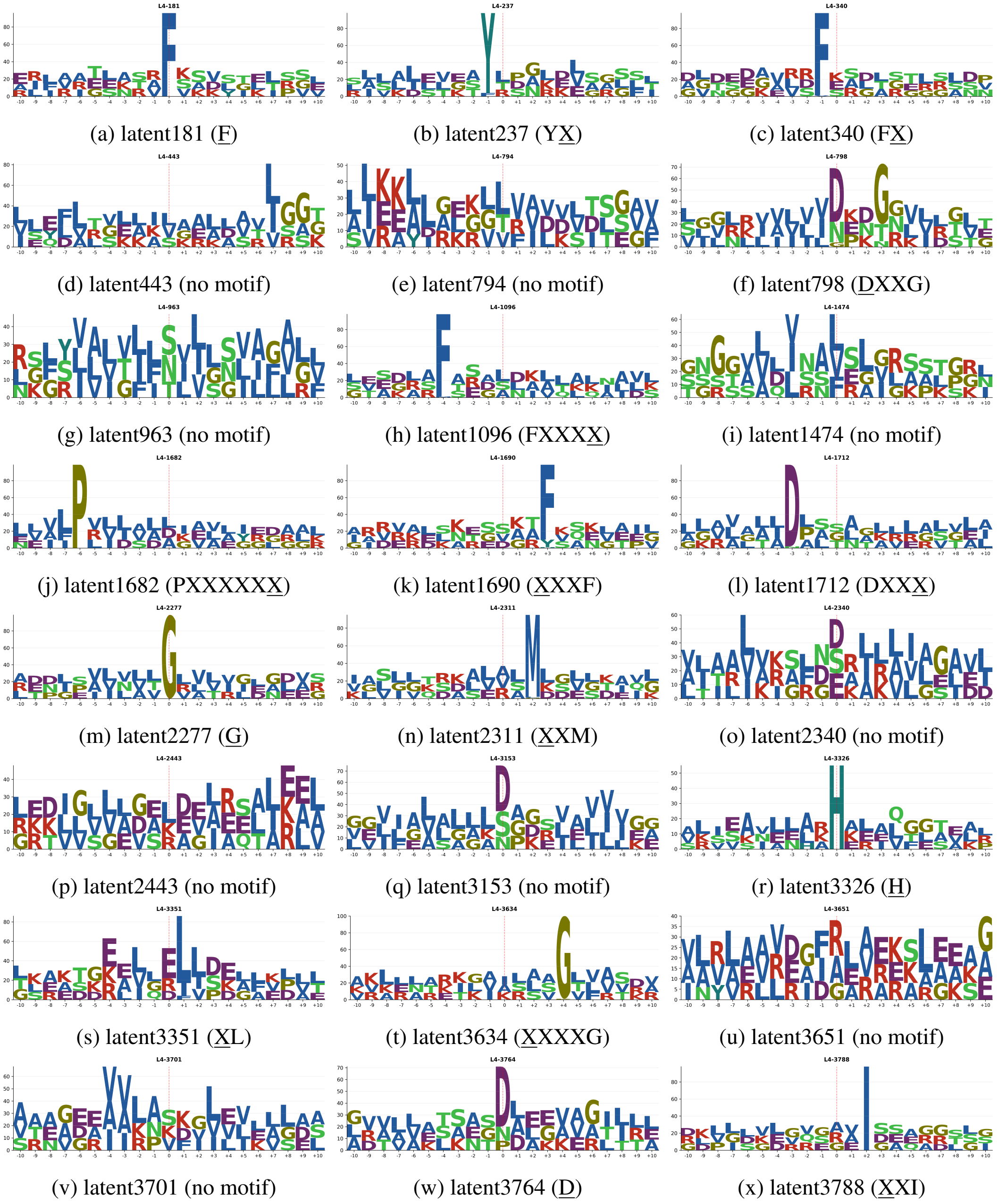

(a) latent181 (F)

(b) latent237 (YX)

(c) latent340 (FX)

(d) latent443 (no motif)

(e) latent794 (no motif)

(f) latent798 (DXXG)

(g) latent963 (no motif)

(h) latent1096 (FXXXX)

(i) latent1474 (no motif)

(j) latent1682 (PXXXXXX)

(k) latent1690 (XXXF)

(l) latent1712 (DXXX)

(m) latent2277 (G)

(n) latent2311 (XXM)

(o) latent2340 (no motif)

(p) latent2443 (no motif)

(q) latent3153 (no motif)

(r) latent3326 (H)

(s) latent3351 (XL)

(t) latent3634 (XXXXG)

(u) latent3651 (no motif)

(v) latent3701 (no motif)

(w) latent3764 (D)

(x) latent3788 (XXI)

Figure 5: Sequence logos for motif-detector latents in layer 4 for MetXA. Each panel shows the 21-residue window centered on the max-activating token; y-axis is information (bits).

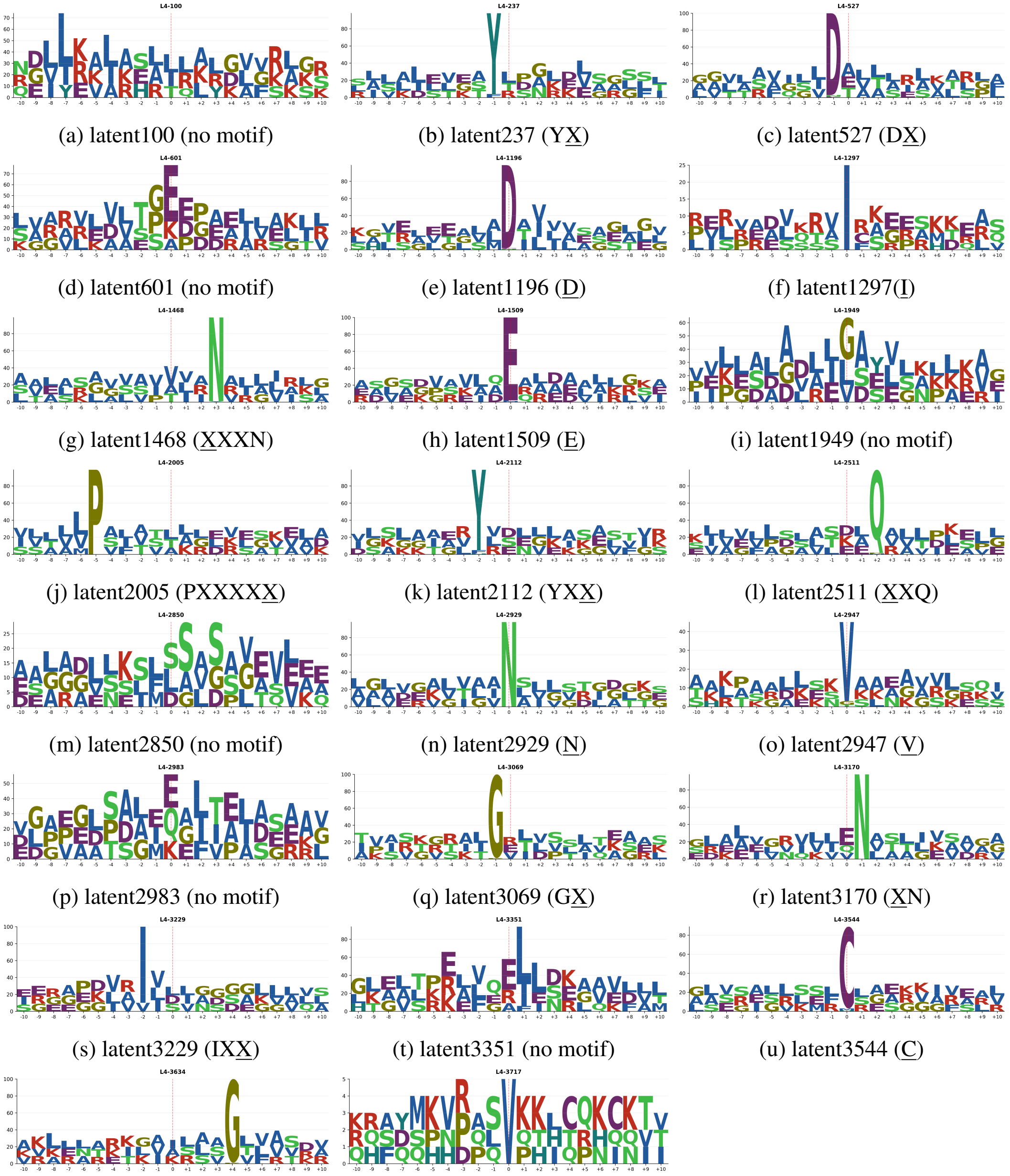

(a) latent100 (no motif)

(b) latent237 (YX̲)

(c) latent527 (DX̲)

(d) latent601 (no motif)

(e) latent1196 (D̲)

(f) latent1297(I̲)

(g) latent1468 (X̲XXN)

(h) latent1509 (E̲)

(i) latent1949 (no motif)

(j) latent2005 (PXXXXX̲)

(k) latent2112 (YXX̲)

(l) latent2511 (X̲XQ)

(m) latent2850 (no motif)

(n) latent2929 (N̲)

(o) latent2947 (V̲)

(p) latent2983 (no motif)

(q) latent3069 (GX̲)

(r) latent3170 (X̲N)

(s) latent3229 (IXX̲)

(t) latent3351 (no motif)

(u) latent3544 (C̲)

(v) latent3634 (X̲XXXG)

(w) latent3717 (V̲)

Figure 6: Sequence logos for motif-detector latents in layer 4 for TOP2. Each panel shows the 21-residue window centered on the max-activating token; y-axis is information (bits).

D Domain Correlation Tables

Table 5: Top domain selectivity latents by AUC for aggregator top-q, group MetXA. We show the number of positive and negative samples, bootstrap 95% CI, Spearman rho correlation of the score vs length of sample.

layer	latent	domain	domain_name	N_pos	N_neg	AUC	CI_lo	CI_hi	rho_len_pos	rho_len_neg
12	3035	IPR036322	WD40	2148	2174	0.997	0.995	0.999	-0.496	0.031
12	2112	IPR029058	AB hydrolase fold	2937	2957	0.994	0.992	0.996	0.075	-0.101
8	2677	IPR036188	FAD/NAD	4014	4124	0.983	0.98	0.985	-0.659	-0.127
12	3536	IPR029063	SAM MTases	10228	10545	0.972	0.97	0.975	-0.388	0.089
8	488	IPR029058	AB hydrolase fold	2937	2957	0.971	0.967	0.975	-0.56	0.089
12	3794	IPR029063	SAM MTases	10228	10545	0.968	0.966	0.971	-0.662	-0.023
12	1256	IPR016181	NAT	1554	1579	0.96	0.951	0.968	-0.271	0.088
12	2797	IPR013785	Aldolase	12702	13012	0.929	0.926	0.932	-0.482	0.036
8	2775	IPR009014	Transketolase	772	785	0.921	0.903	0.937	0.144	-0.047
8	2166	IPR024072	DHFR	135	142	0.86	0.815	0.902	-0.578	0.033

Table 6: Top domain selectivity latents by AUC for aggregator top-q, group TOP2. We show the number of positive and negative samples, bootstrap 95% CI, Spearman rho correlation of the score vs length of sample.

layer	latent	domain	domain_name	N_pos	N_neg	AUC	CI_lo	CI_hi	rho_len_pos	rho_len_neg
12	2472	IPR036961	Kinesin	221	222	0.998	0.992	1	-0.292	-0.028
16	3077	IPR036890	HATPase_C_sf	1700	1737	0.997	0.995	0.999	-0.53	0.011
16	1353	IPR036890	HATPase_C_sf	1700	1737	0.996	0.994	0.998	-0.606	0.013
16	1814	IPR036890	HATPase_C_sf	1700	1737	0.996	0.993	0.998	-0.206	0.091
12	1145	IPR036890	HATPase_C_sf	1700	1737	0.996	0.993	0.998	-0.356	-0.047
20	2311	PF13589	HATPase_c_3	869	892	0.995	0.992	0.999	0.076	0.048
12	3943	IPR036890	HATPase_C_sf	1700	1737	0.995	0.993	0.997	-0.588	0.058
12	1796	IPR036890	HATPase_C_sf	1700	1737	0.994	0.991	0.997	-0.107	0.115
12	1082	PF00867	XPG_I	220	223	0.994	0.983	1	-0.062	-0.055
16	1166	PF13589	HATPase_c_3	869	892	0.992	0.987	0.997	0.135	0.015
12	1204	IPR036890	HATPase_C_sf	1700	1737	0.974	0.969	0.978	0.409	0.094
16	1597	IPR036890	HATPase_C_sf	1700	1737	0.794	0.778	0.811	0.487	0.077
16	3994	PF13589	HATPase_c_3	869	892	0.712	0.685	0.739	0.124	0.007

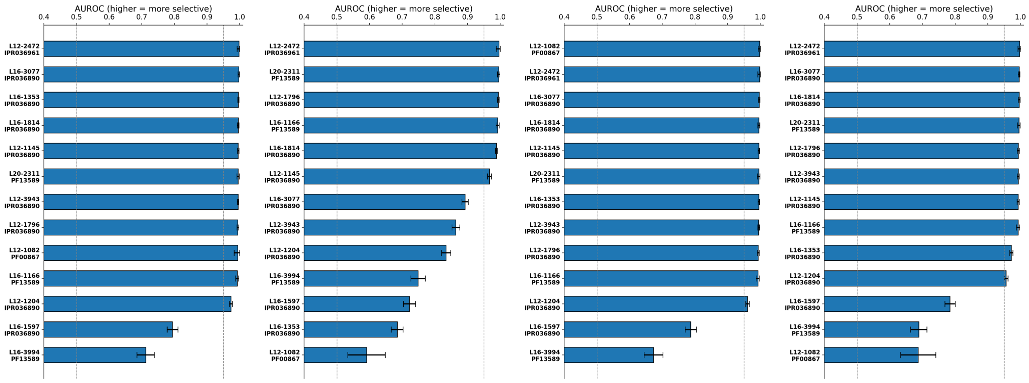

(a) auc topq, top2

(b) auc mean, top2

(c) auc max, top2

(d) auc topk, top2

Figure 7: AUROC score bar charts for TOP2 using mean, max and topk aggregators.

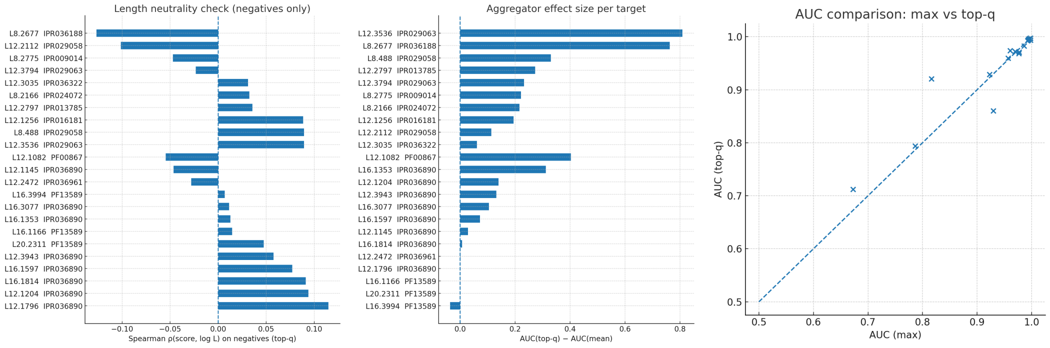

(a) (b) (c)

Figure 8: (a) Spearman rho correlation topq score vs log L, for negative samples between -0.1 to 0.1. (b) Demonstrating difference in auroc for mean and top q%. (c) AUC comparison max vs top q%.

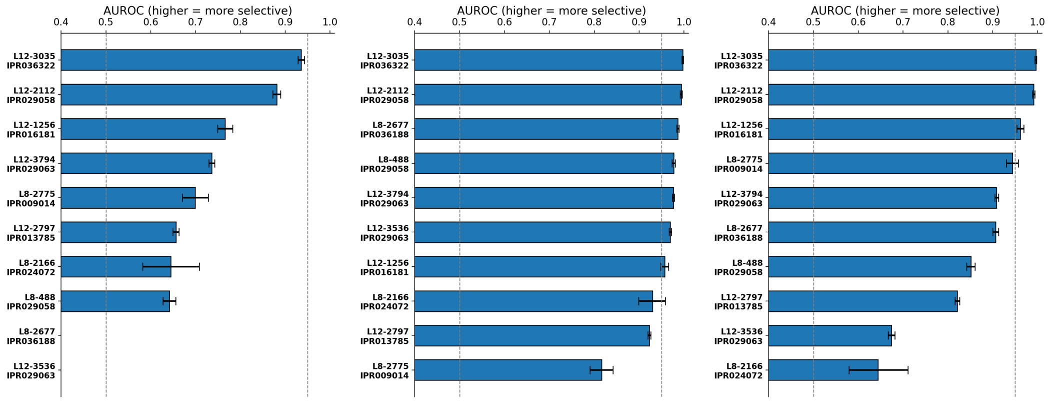

(a) auc mean, metx (b) auc max, metx (c) auc topk, metx

Figure 9: AUROC score bar charts for MetXA using mean, max and topk aggregators.

E Path Patching results

Table 7: Interpretable edges for MetXA between manually analyzed latents. Upstream is earlier, downstream is later.

Edge Rank	Up Layer	Up Latent	Up Feature	Down Layer	Down Latent	Down Feature
19	4	1690	XXXF	8	2775	Transketolase
26	4	798	DXXG	8	2775	Transketolase
47	8	2775	Transketolase	12	1256	FAM
67	8	2775	Transketolase	12	2112	AB_Hydrolase_fold
76	8	2677	FAD/NAD	12	2112	AB_Hydrolase_fold
129	8	2677	FAD/NAD	12	1256	FAM
132	4	340	FX	12	2112	AB_Hydrolase_fold
146	4	2277	G	8	2677	FAD/NAD
147	4	237	YX	8	2775	Transketolase
152	4	3788	XXI	12	2112	AB_Hydrolase_fold
159	4	3788	XXI	12	1256	FAM
168	8	488	AB_Hydrolase_fold	12	2112	AB_Hydrolase_fold
178	8	2677	FAD/NAD	12	2797	Aldolase
179	4	340	FX	12	1256	FAM
184	8	2775	Transketolase	12	2797	Aldolase
186	8	2677	FAD/NAD	12	3794	SAM_mtases
196	8	2677	FAD/NAD	12	3536	SAM_mtases
208	4	3634	XXXXG	8	2677	FAD/NAD
210	4	1690	XXXF	8	2677	FAD/NAD
228	4	3788	XXI	8	2166	DHFR
235	8	2775	Transketolase	12	3536	SAM_mtases
246	4	1690	XXXF	12	1256	FAM
254	4	2311	XXM	12	2112	AB_Hydrolase_fold
268	4	237	YX	12	2112	AB_Hydrolase_fold
274	4	340	FX	8	488	AB_Hydrolase_fold
290	8	2775	Transketolase	12	3035	WD40
295	8	2166	DHFR	12	3536	SAM_mtases
306	4	1682	PXXXXXX	12	1256	FAM

Table 8: Interpretable edges for TOP2 between manually analyzed latents. Upstream is earlier, downstream is later.

Edge Rank	Up Layer	Up Latent	Up Feature	Down Layer	Down Latent	Down Feature
1	12	3943	Hatpase_C	16	1353	Hatpase_C
25	12	1204	Hatpase_C	16	1166	Hatpase_C
28	12	1204	Hatpase_C	16	1597	Hatpase_C
32	12	1796	Hatpase_C	16	1353	Hatpase_C
34	4	1509	E	16	1353	Hatpase_C
40	12	3943	Hatpase_C	16	1597	Hatpase_C
46	4	1509	E	16	1166	Hatpase_C
48	12	1796	Hatpase_C	16	1597	Hatpase_C
54	4	1509	E	12	3943	Hatpase_C
55	4	1509	E	16	1597	Hatpase_C
57	4	3170	XN	12	3943	Hatpase_C
61	4	3170	XN	16	1597	Hatpase_C
66	4	3170	XN	16	1166	Hatpase_C
68	4	2112	YXX	12	2472	Kinesin
76	4	2511	XXQ	12	2472	Kinesin
79	4	2511	XXQ	16	1166	Hatpase_C
82	4	2929	N	12	2472	Kinesin
87	4	527	DX	12	2472	Kinesin
91	4	3717	V	12	2472	Kinesin
92	4	1468	XXXN	12	2472	Kinesin
100	4	3717	V	16	1597	Hatpase_C
102	4	3170	XN	12	2472	Kinesin
118	4	3069	GX	16	1353	Hatpase_C
123	4	3717	V	16	1166	Hatpase_C
137	12	1204	Hatpase_C	16	1353	Hatpase_C
140	4	1509	E	12	1796	Hatpase_C
151	12	2472	Kinesin	16	1597	Hatpase_C
157	4	1468	XXXN	12	3943	Hatpase_C
175	4	3170	XN	16	1353	Hatpase_C
189	4	527	DX	16	1166	Hatpase_C
198	4	3069	GX	12	1204	Hatpase_C
203	4	1468	XXXN	16	1353	Hatpase_C
204	4	1468	XXXN	16	1597	Hatpase_C
223	12	2472	Kinesin	16	1166	Hatpase_C
225	4	1468	XXXN	16	1166	Hatpase_C
229	4	3069	GX	16	1166	Hatpase_C
232	4	3544	C	12	1204	Hatpase_C
234	4	1297	I	16	1597	Hatpase_C
238	4	3544	C	12	3943	Hatpase_C

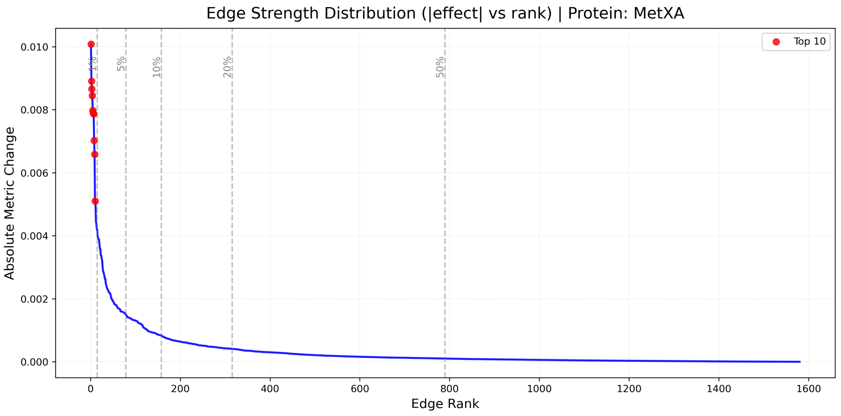

Figure 10: Edge strength distribution (sorted by $|\Delta m|$) for MetXA.

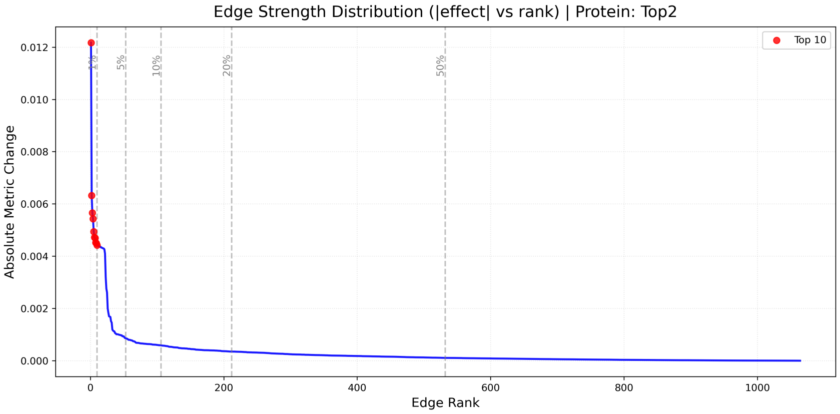

Figure 11: Edge strength distribution (sorted by $|\Delta m|$) for TOP2.

F Additional recovery curves

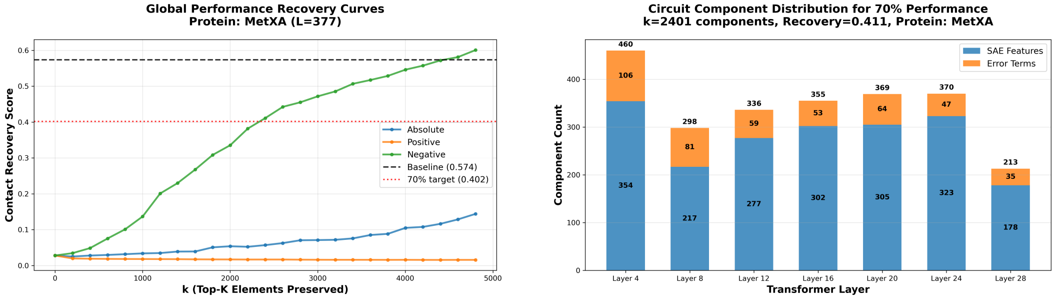

(a) Global recovery curve - MetXA

(b) Circuit size distribution - MetXA

Figure 13: Performance and distribution diagnostics for the learned circuit.

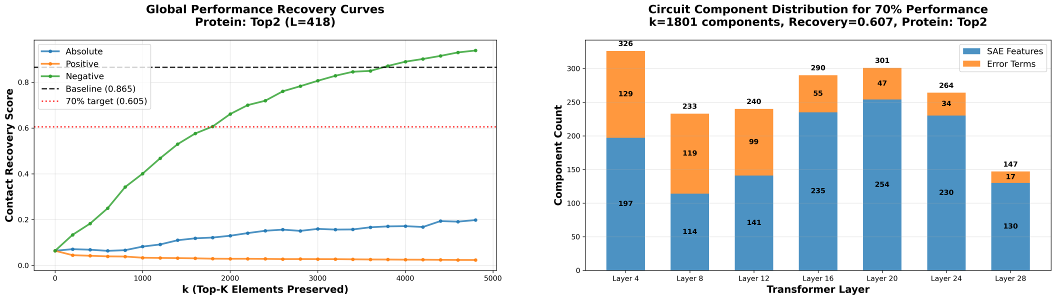

(a) Global recovery curve - TOP2

(b) Circuit size distribution - TOP2

Figure 14: Performance and distribution diagnostics for the learned circuit.